

A statistical boundary layer model for the mantle D'' region

Benjun Wu,¹ Peter Driscoll,¹ and Peter Olson²

Received 7 May 2011; revised 18 October 2011; accepted 21 October 2011; published 30 December 2011.

[1] The D'' region above the core-mantle boundary (CMB) plays critical roles in the dynamics of both the mantle and the core; however, the complexity of this region observed over a broad range of spatial scales defies simple interpretations as either purely thermal or purely chemical heterogeneity. Here, we formulate a 1-D, time-dependent boundary layer model for the D'' region, which provides statistical properties of the dynamics and seismic heterogeneity, by coupling thermal, chemical, and phase (TCP) variability in the layer. We assume a Gaussian-like time-dependent mantle flow, compositional stratification due to variations in iron content, heat flow variations because of changes in the local temperature gradient, and a postperovskite (PPV) phase transformation. We compute a range of TCP boundary layer model cases that are consistent with the observed seismic shear wave velocity heterogeneity in the region 50–300 km above the CMB. These results imply an average CMB heat flow near 13 TW with ± 3 TW variations, CMB temperature of 4000 K, a large positive PPV Clapeyron slope, and an average heat transport of about 3 TW associated with deep mantle plumes.

Citation: Wu, B., P. Driscoll, and P. Olson (2011), A statistical boundary layer model for the mantle D'' region, *J. Geophys. Res.*, 116, B12112, doi:10.1029/2011JB008511.

1. Introduction

[2] The core-mantle boundary (CMB) separating the silicate-oxide mantle and the metallic outer core is the most fundamental transition in the interior of the Earth. The D'' layer was originally defined [Bullen, 1949] to include several hundred kilometers of the lowermost mantle above the CMB. It is now known to contain large amplitude seismic heterogeneity over a wide spectrum of scales (see reviews by Garnero [2000] and Lay et al. [1998]), indicating a multitude of overlapping dynamical processes.

[3] Traditionally, the heterogeneity in D'' is explained by the large thermal gradients associated with a thermal boundary layer (TBL), in which the heat from the core is transferred across the CMB by thermal conduction and is a vital component of the energy budget for mantle and core convection [Jaupart et al., 2007; Lay et al., 2008]. More recently, the heterogeneous structures in D'' are interpreted by postulating a chemical boundary layer (CBL) in addition to the TBL [McNamara and Zhong, 2005; Tackley, 2002]. Evidence for the compositional heterogeneity in D'' region includes the observed anticorrelation between the elastic shear modulus and bulk modulus inferred from seismic tomography [Masters et al., 2000; Trampert et al., 2004] and the massive scale of the low-seismic velocity structures beneath Africa and the South Pacific [Ishii and Tromp, 2004; Trampert et al., 2004]. However, the composition of

this heterogeneity remains uncertain; proposals include anomalous iron and silica content [Deschamps et al., 2007].

[4] In addition, high-pressure mineral physics results argue for heterogeneity from one or more phase transitions within this region. The most important solid-state phase transition is the transformation of silicate perovskite (PV) to the denser postperovskite (PPV) phase [Murakami et al., 2004]. Both experiments and theory [Hutko et al., 2008; Lay et al., 2006; Oganov and Ono, 2004; Tsuchiya et al., 2004; van der Hilst et al., 2007; Wentzcovitch et al., 2006] indicate that the PV–PPV phase transition occurs within a depth range of several hundred kilometers above the CMB, which is broadly compatible with the location of a known seismic discontinuity at the top of D'' region [Lay and Helmberger, 1983; Wysession et al., 1998]. A reverse transition from PPV back to PV may be present close to the CMB because of the higher temperatures there, which generates a double-crossing structure [Hernlund et al., 2005].

[5] Furthermore, abundant seismic evidences suggest finer-scale heterogeneity and anisotropy in the D'' region. In particular, thin lenses with strongly reduced compression and shear wave velocity, the so-called ultralow velocity zones (ULVZ), have been imaged just above the CMB [Garnero and Helmberger, 1996]. The physical and chemical nature of the ULVZ is obscure, although partial melting of mantle silicates is the favored interpretation [e.g., Lay et al., 2004; Williams and Garnero, 1996].

[6] Global-scale dynamical models emphasize the role of D'' region as the basal thermo-chemical boundary layer in mantle convection, including its role in core heat loss [e.g., Labrosse, 2002], deep mantle plume formation leading to large igneous provinces and volcanic hot spots [e.g., Burke and Torsvik,

¹Department of Geology and Geophysics, Yale University, New Haven, Connecticut, USA.

²Department of Earth and Planetary Sciences, Johns Hopkins University, Baltimore, Maryland, USA.

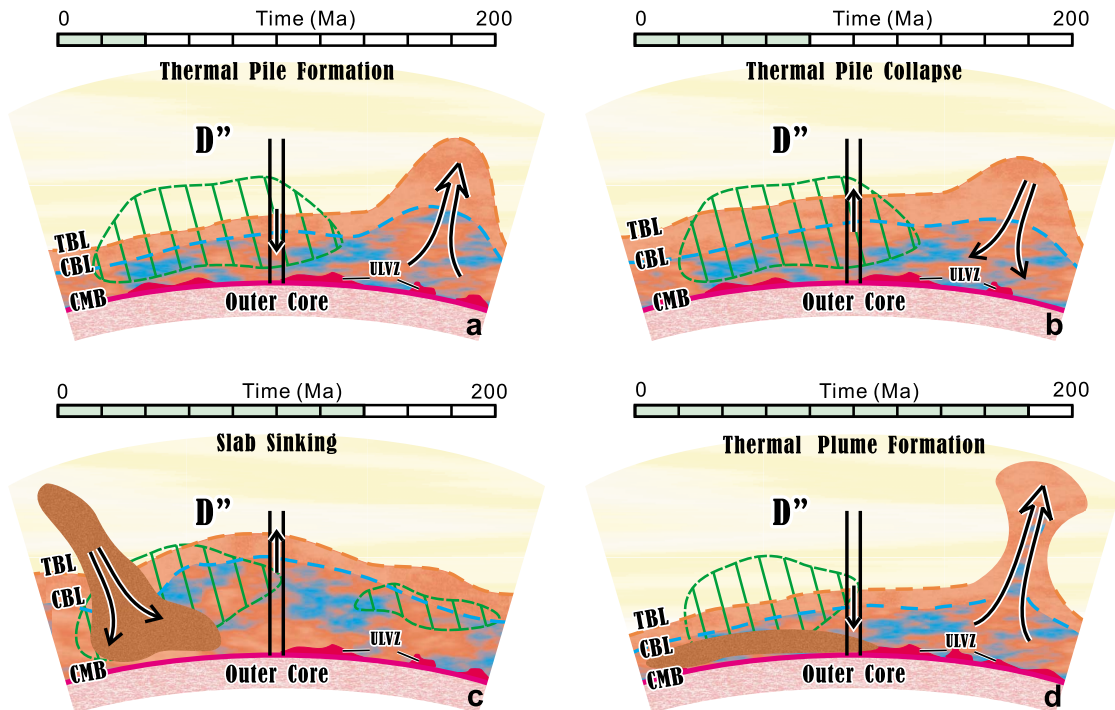


Figure 1. Four dynamical stages in the D'' region are represented in the TCP model. The thickest red layer represents the part of the TBL (red dash line) that extends above the chemically dense layer (blue dash line) with its higher iron content (blue). Green regions indicate the PPV phase. Arrows are the direction of lower mantle flows. The vertical lines denote the measurement location P. (a) Growth of a thermochemical pile drains the D'' region. (b) Collapse of a thermochemical pile floods the D'' layer. (c) Addition of subducted lithosphere material floods the D'' region. (d) Thermal plume formation drains the upper portion of the D'' region. The time line above each stage indicates the approximate order of these events in a 200 Ma sequence. Following thermal plume detachment in the fourth stage (Figure 1d) the layer returns to first stage (Figure 1a).

2004], and as a graveyard for subducted slabs [e.g., *Hutko et al.*, 2006; *van der Hilst et al.*, 1997]. Small-scale local models argue the D'' region is the site of instabilities [e.g., *Hansen and Yuen*, 1988], partial melting [e.g., *Williams and Garnero*, 1996] and possible mass exchange with the core [e.g., *Knittle and Jeanloz*, 1991]. From the perspective of the core, the D'' layer represents a variable heat transfer boundary condition that may affect the long-term behavior of the geodynamo [Buffett, 2002; Lay and Garnero, 2004] and may influence the growth of the inner core [Buffett, 2003; Labrosse et al., 2001; Lay et al., 2008].

[7] In this article, we formulate an analytical boundary layer model for the D'' region that connects its dynamics to statistical properties of observed seismic heterogeneity. The model is based on ideas originally proposed by Howard [1964] for the statistics of plume formation from a turbulent boundary layer in high Rayleigh number thermal convection. The original Howard model, which is 1-D in space and time dependent, considered only thermal effects. We extend Howard's formulation to include chemical and phase variations. The model is applied to the D'' layer as a superposition of TBL, CBL, PPV phase change, so-called thermal, chemical, and phase (TCP) boundary layer model. The objective of the TCP model is to incorporate seismic constraints on important dynamical properties such as CMB heat

flow amplitude, heterogeneity, thermal and chemical boundary layer thickness, and deep mantle plume flux.

2. TCP Model

2.1. Model Setup

[8] With TCP heterogeneities contributing to the flow, D'' layer dynamics are likely to be spatially complex and highly time dependent. To allow for complex lower mantle forcing in an analytical model, we consider the vertical motion of the D'' layer flow at a fixed (latitude and longitude) location P in the four stages shown in Figure 1. These stages are similar to experiments performed by Kumagai et al. [2008], which show an oscillating superplume behavior. In Figure 1a, a thermochemical pile away from P is growing, where buoyancy and pressure forces lift the material from the base of the layer to concentrate a large pile of intrinsically dense material. The growth of this pile partially drains the rest of the layer, and the radial motion at P is downward at this stage. The pile growth is stalled when negative buoyancy exceeds the upward forces acting on it, the pile collapses, and the dense material flows back into the CBL (Figure 1b), and the radial motion at P is upward. In the next stage, subducted slab material descends to the base of the mantle and is incorporated into the D'' region. As the new material

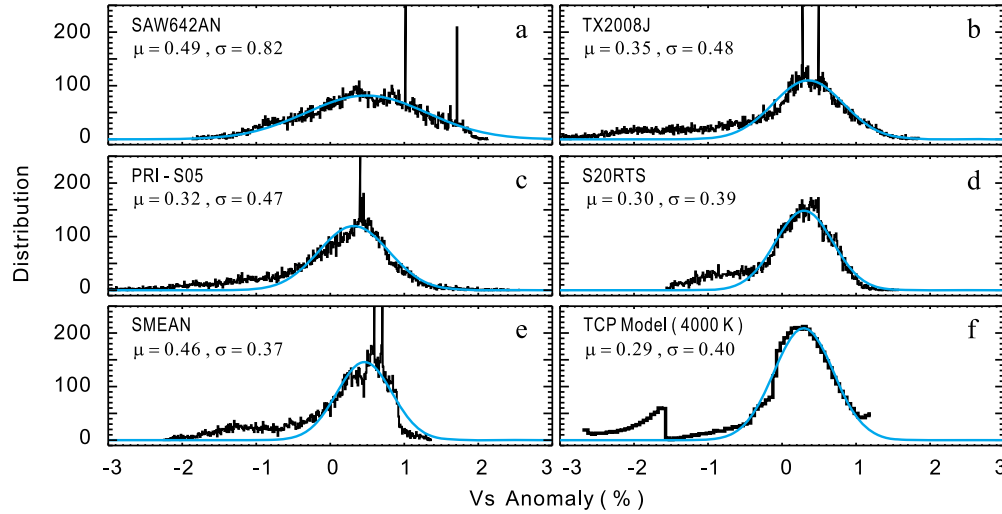


Figure 2. Seismic shear wave velocity V_S heterogeneity statistics at a depth of 2750 km. (a–e) Labeled seismic tomography models and (f) the shear wave heterogeneity statistics from the TCP model case C4014_0511. Blue curves are Gaussian fits to the main peaks of the distributions.

is added to the layer, flow at point P is upward, away from the CMB (Figure 1c). The final stage is the thermal plume formation, illustrated in Figure 1d. As the TBL thickens by diffusion and by the addition of subducted slab material, Rayleigh-Taylor instabilities develop at the most unstable wave number, which grow into the thermal plumes that rise up into mantle. The effect of plume formation is to partially drain the D'' region of thermal buoyancy, inducing downward flow toward the CMB at location P. We assume that the motion at a particular location P in the D'' layer is remote from the most active regions where subducted material is added and plume material is lost, and the variations described here have a periodicity of 200 Ma [Courtillot and Olson, 2007; Maruyama et al., 2007].

[9] The essence of Howard's [1964] thermal plume model is that time averages at a fixed location in the boundary layer are equivalent to spatial averages over the boundary layer at a fixed time. Assuming this is applicable in the mantle, constraints on the time dependence of the D'' region can be found in the present-day statistical distribution of D'' region seismic heterogeneity. Figure 2 shows the distributions of seismic shear wave velocity (V_S) heterogeneity at 2750 km depth from several lower mantle seismic tomography models SAW642AN [Panning and Romanowicz, 2006], TX2008J [Simmons et al., 2009], PRI-S05 [Montelli et al., 2006], S20RTS [Ritsema et al., 2004], and SMEAN, with Gaussian curves fit to each. Model SMEAN, an average S wave model, is constructed by averaging the heterogeneity structure of the four individual tomography models, distributed on a $2^\circ \times 2^\circ$ grid in latitude and longitude. The statistical distributions of the seismic heterogeneity have nearly Gaussian modes with comparable means and standard deviations. Accordingly, we choose a velocity time dependence for the TCP boundary layer model that gives approximately Gaussian statistics. Figure 2f shows the example of synthetic V_S distributions from the TCP models.

2.2. TBL Statistics

[10] Heat transfer in D'' region is calculated as a function of time using the following 1-D heat transport equation:

$$\frac{\partial T}{\partial t} + w \frac{\partial T}{\partial z} = \kappa \frac{\partial^2 T}{\partial z^2}, \quad (1)$$

where T is temperature, t is time, w is vertical velocity, κ is thermal diffusivity, and z is height above the CMB. The definitions of all symbols are listed in Table 1. Here we have eliminated horizontal advection terms because they are small compared to radial. We also ignored the contribution of phase transformations in the heat balance, as they are uncertain. The vertical velocity $w(z, t)$ describes the time-dependent motion in the boundary layer. Assuming a stagnation flow above the stress-free CMB, the vertical velocity is

$$w(z, t) = -zf(t). \quad (2)$$

The function $f(t)$ with units s^{-1} represents the downwelling intensity at location P; the choice of this function determines the heterogeneity properties of D'' and links the heterogeneity of the TBL to that in the CBL.

[11] The main requirement on f is that it should give a Gaussian distribution for the boundary layer thermal heterogeneity that is similar to the observed Gaussian-like distribution of the V_S heterogeneity in D'' . However, it is difficult to find a general form of the function $f(t)$ that produces a Gaussian-like velocity heterogeneity, because of the nonlinear relationship between f and V_S . In this study, we focus on a particular choice of the function $f(t)$, which is periodic and analytic, with only two parameters, and yields a nearly Gaussian distribution of velocity heterogeneity. The value of f is assumed to vary in time like

$$f^* = f_0 + \frac{1}{f_1 \sin(2\pi t^*)}, \quad (3)$$

Table 1. Definition of Symbols

Symbol	Definition	Units (Commonly Used Units or Value)
A^*	Nondimensional form of variables	
f	Downwelling rate	s^{-1}
f_0 and f_1	Amplitude coefficients of downwelling rate	
h	CBL thickness	km
M	Misfit	
q	Heat flux	$W m^{-2}$
q_{CMB}	CMB heat flux	$W m^{-2}$
\bar{q}_{CMB}	Mean CMB heat flux	$W m^{-2}$
$d\ln q_{CMB}$	CMB heat flux anomaly	%
Q_{CMB}	CMB heat flow	W
\bar{Q}_{CMB}	Mean CMB heat flow	W
Q_{plume}	Plume heat flow	W
σ_Q	Standard deviation of CMB heat flow	W
t	Time	s
T	Temperature	K
T_{CMB}	Temperature at the CMB	K
T_{diff}	Contrast of T and T_{PPV} at certain height	K
T_{diff_min}	Minimum of the contrast of T and T_{PPV}	K
T_{int}	Temperature of PPV boundary at the CMB	K
T_{LM}	Lower mantle temperature	K
T_{PPV}	Temperature of PPV phase transition boundary	K
ΔT	Temperature difference between the lower mantle and the CMB	K
\bar{T}	Mean temperature	K
T'	Temperature anomaly	K
T'^2	Temperature variance	
V_S	Seismic shear wave velocity	$m s^{-1}$
$d\ln V_S$	Seismic shear wave velocity anomaly	%
σ_V	RMS variation of V_S	%
σ_{V^*}	RMS variation of observed V_S	%
w	Vertical velocity	$m s^{-1}$
z	Height above CMB	km
$z_{critical}$	Critical height for PPV single-crossing structure	km
z_{diff}	Height corresponding to T_{diff}	km
z_{ref}	Height of PPV boundary reference point	km
γ	Clapeyron slope	$Pa K^{-1}$
δ	TBL thickness	km
δ_{btm}	Minimum TBL thickness	km
δ_{top}	Maximum TBL thickness	km
$\bar{\delta}$	Mean TBL thickness	km
σ_δ	Standard deviation of TBL thickness	km
$\delta_{critical}$	Critical TBL thickness for PPV presence	km
ϕ_{PPV}	Fraction of PPV phase	%
ϕ'_{PPV}	PPV phase anomaly	%
ϕ'^2_{PPV}	PPV phase variance	
χ_{Fe}	Fraction of dense material	%
χ'_{Fe}	Dense material anomaly	%
χ'^2_{Fe}	Dense material variance	
$\langle \tau \rangle$	Total time region	
$\langle \tau_{CBL} \rangle$	Time region with CBL	
$\langle \tau_{xCBL} \rangle$	Time region without CBL	
τ_{xCBL}	Length of time without CBL	s
$\langle \tau_{PPV} \rangle$	Time region with PPV	
$\langle \tau_{xPPV} \rangle$	Time region without PPV	
τ_{xPPV}	Length of time without PPV	s
C_p	Thermal capacity	$1250 J kg^{-1} K^{-1}$
F_{PV}	Fraction of PV in the D'' region	75%
g	Gravitational acceleration	$10.5 m \cdot s^{-1}$
h_0	Reference CBL thickness	150 km
k	Thermal conductivity	$10 W K^{-1} m^{-1}$
R_{CMB}	Radius of CMB	3480 km
T_{ref}	Temperature of PPV boundary reference point	2500 K
$\Delta V_{S_{PV \rightarrow PPV}}$	Velocity change from PV to PPV	1.5%
κ	Thermal diffusivity	$1.45 \times 10^{-6} m^2 s^{-1}$
ρ_m	Density of lower mantle	$5500 kg m^{-3}$
$\Delta \rho_c$	Density difference of dense material	$55 kg m^{-3}$
τ	Typical geological plume time	200 Ma
χ_0	Fraction of dense material at the top of CBL	0.1

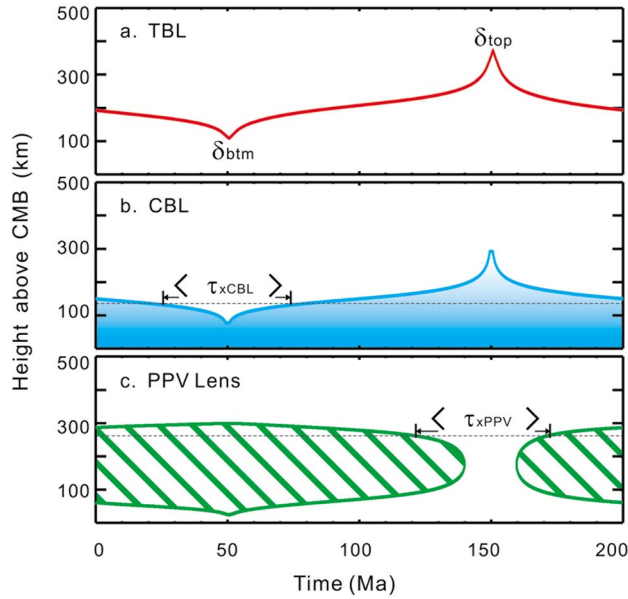


Figure 3. Time variation of the TCP boundary layers from the case C4014_0511 that yield Gaussian-like statistics. (a) TBL thickness, (b) CBL thickness, and (c) PPV lens locations.

where $f^* = f\tau$ and $t^* = t/\tau$, where $*$ denotes dimensionless quantities and $\tau = 200$ Ma is the assumed periodicity of the event sequence shown in Figure 1. The second term in equation (3) is numerically limited to a maximum value to avoid the singularity where the sine function vanishes. As shown in the following, the amplitude coefficients f_0 and f_1 in equation (3) are the most sensitive parameters that control the statistical properties of the mantle flow in the D'' region.

[12] The heat transport equation (1) is subject to half-space thermal boundary conditions, with $T = T_{LM}$ the temperature of the lower mantle at $z = \infty$ and $T = T_{CMB}$ at the CMB $z = 0$, which is assumed to be isothermal. In terms of the temperature difference between the lower mantle and the CMB

$$\Delta T = T_{CMB} - T_{LM}, \quad (4)$$

the temperature variation in the D'' layer, the analytical solution of equation (1), can be written as

$$T = T_{CMB} - \Delta T \operatorname{erf}\left(\frac{z}{\delta(t)}\right), \quad (5)$$

where δ is the TBL thickness. Substituting equations (2)–(5) into equation (1), the heat equation reduces to an evolution equation for $\delta(t)$,

$$f\delta^2 + \delta \frac{d\delta}{dt} - 2\kappa = 0. \quad (6)$$

Figure 3a shows an example of how the TBL thickness δ varies as a function of time, obtained by solving equation (6) with $f_0 = 0.5$ and $f_1 = 1.1$ using a fourth-order Runge-Kutta method.

[13] The temperature anomaly $T'(z, t)$ is defined as the difference between $T(z, t)$ and its time average at a height z , $\bar{T}(z)$, which is given by

$$T' = T - \bar{T} = \Delta T \left[\frac{1}{\tau} \int_0^\tau \operatorname{erf}\left(\frac{z}{\delta(t)}\right) dt - \operatorname{erf}\left(\frac{z}{\delta(t)}\right) \right]. \quad (7)$$

Using equation (7), we form the variance of the boundary layer temperature $\overline{T'^2}(z)$ by taking the mean square of T' over time, which is only a function of the height above the CMB:

$$\begin{aligned} \overline{T'^2} &= \frac{1}{\tau} \int_0^\tau T'^2 dt = \Delta T^2 \left[- \left(\frac{1}{\tau} \int_0^\tau \operatorname{erf}\left(\frac{z}{\delta(t)}\right) dt \right)^2 \right. \\ &\quad \left. + \frac{1}{\tau} \int_0^\tau \left(\operatorname{erf}\left(\frac{z}{\delta(t)}\right) \right)^2 dt \right]. \end{aligned} \quad (8)$$

2.3. CBL Statistics

[14] We assume an anomalously high-density material with thickness $h(t)$ located between the CMB and the top of the TBL. In the following calculations, the anomalous chemical composition is assumed to have a higher iron content compared to the rest of the lower mantle, although the method can be adjusted to accommodate any dense constituent. We also assume that the CBL responds to the same vertical motions as the material in the TBL, so the motion of the top of the CBL is given by

$$\frac{dh}{dt} = w \quad (\text{at } z = h). \quad (9)$$

Denoting by h_0 , the reference CBL thickness at the beginning of each cycle, equations (2), (3), and (9) yield

$$h(t) = h_0 |\tan \pi t^*|^{-\frac{1}{2f_1}}. \quad (10)$$

In this study, h_0 is assumed to be 150 km [Simmons and Grand, 2002; Wang and Wen, 2004]. In deriving equation (10), we have assumed that the chemical layer is a closed system, in which no dense material enters or leaves, so that we can set $f_0 = 0$ when applying equation (3) to equation (9). Figure 3b shows the resulting time-dependent CBL thickness according to equation (10) with $f_1 = 1.1$.

[15] To calculate the statistics of the compositional heterogeneity, we denote $\chi_{Fe}(z, t)$ the volume fraction of dense material as a function of time and height, so that $\chi_{Fe} = 0$ corresponds to iron-free material, and $\chi_{Fe} > 0$ corresponds to iron enriched material. We assume that the iron content is a linearly decreasing function of z , so that $\chi_{Fe} = 1$ at CMB and $\chi_{Fe} = \chi_0$ at the top of CBL. In most cases, $\chi_0 = 0.1$. The notation $\langle \rangle$ is used to indicate different portions of the time cycle. The notation $\langle \tau_{xCBL} \rangle$ denotes a time interval in which dense material is absent, $\langle \tau \rangle$ denotes the entire time cycle with the length of τ , and $\langle \tau_{CBL} \rangle = \langle \tau \rangle - \langle \tau_{xCBL} \rangle$ denotes the time interval in which dense material is present. The variable

$\tau_{x\text{CBL}}$ is the time length corresponding to $\langle \tau_{x\text{CBL}} \rangle$. In terms of this notation the iron concentration can be written as:

$$\chi_{\text{Fe}}(z, t) = \begin{cases} 0 & , t \in \langle \tau_{x\text{CBL}} \rangle \\ 1 + \frac{\chi_0 - 1}{h(t)} z & , t \in \langle \tau_{\text{CBL}} \rangle \end{cases} \quad (11)$$

Similar to the temperature anomaly, the anomalous iron concentration χ'_{Fe} is

$$\begin{aligned} \chi'_{\text{Fe}}(z, t) &= \chi_{\text{Fe}} - \overline{\chi_{\text{Fe}}} \\ &= \begin{cases} \frac{1}{\tau} \left(\tau_{x\text{CBL}} - (\chi_0 - 1)z \int_{\langle \tau_{\text{CBL}} \rangle} \frac{1}{h(t)} dt \right) - 1 & , t \in \langle \tau_{x\text{CBL}} \rangle \\ \frac{1}{\tau} \left(\tau_{x\text{CBL}} - (\chi_0 - 1)z \int_{\langle \tau_{\text{CBL}} \rangle} \frac{1}{h(t)} dt \right) + \frac{(\chi_0 - 1)z}{h(t)} & , t \in \langle \tau_{\text{CBL}} \rangle \end{cases} \end{aligned} \quad (12)$$

where $\overline{\chi_{\text{Fe}}}(z)$ is the time average of χ_{Fe} at a height z . The variance $\overline{\chi'_{\text{Fe}}{}^2}(z)$ is then given by

$$\begin{aligned} \overline{\chi'_{\text{Fe}}{}^2} &= \frac{1}{\tau} \int_0^\tau \chi'_{\text{Fe}}{}^2 dt = \frac{1}{\tau} \left[\tau_{x\text{CBL}} + (\chi_0 - 1)^2 z^2 \int_{\langle \tau_{\text{CBL}} \rangle} \left(\frac{1}{h(t)} \right)^2 dt \right] \\ &\quad - \frac{1}{\tau^2} \left[\tau_{x\text{CBL}} - (\chi_0 - 1)z \int_{\langle \tau_{\text{CBL}} \rangle} \frac{1}{h(t)} dt \right]^2 \end{aligned} \quad (13)$$

2.4. PPV Phase Transition

[16] The location of the PPV material, where the local temperature is below that of the PPV phase transformation, can be expressed in terms of the phase equilibrium temperature T_{PPV} and the geotherm. Within the D'' region, a local approximation for T_{PPV} is given by

$$T_{\text{PPV}} = T_{\text{ref}} - \frac{\rho_m g}{\gamma} (z - z_{\text{ref}}), \quad (14)$$

where ρ_m is lower mantle reference density, g is gravitational acceleration (assumed constant), γ is Clapeyron slope of the PPV transition, z_{ref} is reference height above the CMB, and T_{ref} is a reference temperature. In this study, a reference height of $z_{\text{ref}} = 300$ km is chosen so as to be in accord with the average height of the observed seismic velocity discontinuity near the CMB [Hutko et al., 2008; van der Hilst et al., 2007; Wysession et al., 1998], and $T_{\text{ref}} = 2500$ K equals to the lower mantle reference temperature [Boehler, 1996]. Figure 3c shows an example of the location and structure of a PPV lens according to equation (14).

[17] To calculate the PPV phase variation, we used $\phi_{\text{PPV}}(z, t)$ to denote the volume fraction of the PPV phase. As the PPV transition is univariant, there are only two possible values: $\phi_{\text{PPV}} = 1$ corresponding to PPV presence and $\phi_{\text{PPV}} = 0$ corresponding to PPV absence. Denoting by $\langle \tau_{x\text{PPV}} \rangle$ the region where PPV phase is absent, then $\langle \tau_{\text{PPV}} \rangle = \langle \tau \rangle - \langle \tau_{x\text{PPV}} \rangle$ denotes the region where PPV phase is present,

and $\tau_{x\text{PPV}}$ denotes the length of time corresponding to $\langle \tau_{x\text{PPV}} \rangle$. Using this notation,

$$\phi_{\text{PPV}}(z, t) = \begin{cases} 0 & , t \in \langle \tau_{x\text{PPV}} \rangle \\ 1 & , t \in \langle \tau_{\text{PPV}} \rangle \end{cases}, \quad (15)$$

and the anomaly ϕ'_{PPV} written as:

$$\phi'_{\text{PPV}}(z, t) = \phi_{\text{PPV}} - \overline{\phi_{\text{PPV}}} = \begin{cases} \frac{\tau_{x\text{PPV}}}{\tau} - 1 & , t \in \langle \tau_{x\text{PPV}} \rangle \\ \frac{\tau_{x\text{PPV}}}{\tau} & , t \in \langle \tau_{\text{PPV}} \rangle \end{cases}, \quad (16)$$

where $\overline{\phi_{\text{PPV}}}(z)$ is time average of ϕ_{PPV} as a function of height. The PPV phase variance $\overline{\phi'_{\text{PPV}}{}^2}(z)$ is obtained from

$$\overline{\phi'_{\text{PPV}}{}^2}(z) = \frac{1}{\tau} \int_0^\tau \phi'_{\text{PPV}}{}^2 dt = \frac{\tau_{x\text{PPV}}}{\tau} \left(1 - \frac{\tau_{x\text{PPV}}}{\tau} \right). \quad (17)$$

2.5. Seismic Shear Wave Velocity Anomalies

[18] Seismic shear wave velocity anomalies $d \ln V_S$ can be represented in terms of the anomalies in temperature, composition, and PPV phase in the TCP model according to *Trampert et al.* [2004] as follows:

$$d \ln V_S = \frac{\partial \ln V_S}{\partial T} T' + \frac{\partial \ln V_S}{\partial \chi_{\text{Fe}}} \chi'_{\text{Fe}} + \frac{\partial \ln V_S}{\partial \phi_{\text{PPV}}} \phi'_{\text{PPV}}, \quad (18)$$

where T' , χ'_{Fe} , and ϕ'_{PPV} are derived from equations (7), (12), and (16).

[19] In equation (18), the temperature sensitivity coefficient is approximately

$$\frac{\partial \ln V_S}{\partial T} = -2.6 \times 10^{-5}, \quad (19)$$

and the chemical sensitivity coefficient for iron [Trampert et al., 2004] is approximately

$$\frac{\partial \ln V_S}{\partial \chi_{\text{Fe}}} = -1.65 \frac{\Delta \rho_c}{\rho_m} = -1.65 \times 10^{-2}, \quad (20)$$

where $\Delta \rho_c$ is the reference density excess. We assume that $\Delta \rho_c / \rho_m = 0.01$ in calculations. Note that S wave velocity is faster for PPV than for PV, that is, the velocity increases from PV to PPV, $\Delta V_{S_{\text{PV} \rightarrow \text{PPV}}} \cong 1.5 \sim 2\%$ [Oganov and Ono, 2004; Stackhouse et al., 2005; Wentzcovitch et al., 2006; Wookey et al., 2005]. In terms of F_{PV} , the fraction of PV near the CMB (which is about 0.75) [see Deschamps and Trampert, 2004], the PPV phase sensitivity can be approximated as

$$\frac{\partial \ln V_S}{\partial \phi_{\text{PPV}}} = \Delta V_{S_{\text{PV} \rightarrow \text{PPV}}} \cdot F_{\text{PV}} \cong 1.13 \times 10^{-2}. \quad (21)$$

3. Results

[20] In applying this model, we focus on constraining four key physical parameters that have the most significant

Table 2. TCP Model Groups

ΔT (K)	γ (MPa K ⁻¹)				
	8	10	12	14	16
3700	G3708	G3710	G3712	G3714	G3716
4000	G4008	G4010	G4012	G4014	G4016
4300	G4308	G4310	G4312	G4314	G4316

impact on the TCP boundary layer structure: ΔT , γ , f_0 , and f_1 . The temperature difference between the lower mantle and the CMB is currently a matter of debate, so we consider ΔT equal to 1200, 1500, and 1800 K. As the TCP model is applicable in the inactive regions in D'' away from upwellings and downwellings where the lower mantle temperature changes are the largest, we assume a constant value of 2500 K for the lower mantle temperature, which gives T_{CMB} of 3700, 4000, and 4300 K, respectively. In what follows, we refer to these cases as cold, warm, and hot CMB temperatures, respectively.

[21] Experimental phase equilibrium studies [Murakami *et al.*, 2004; Oganov and Ono, 2004; Shim *et al.*, 2004] consistently yield positive Clapeyron slopes γ for the PV to PPV phase transition but with little consensus on its exact value. Accordingly, we examine models with positive Clapeyron slopes corresponding to $\gamma = 8, 10, 12, 14,$ and 16 MPa K^{-1} , respectively. Designations for the 15 different combinations of ΔT and γ are given in Table 2.

[22] The least constrained-free model parameters are the velocity coefficients f_0 and f_1 . Their only numerical constraint in the context of the TCP model is the requirement for a small numerical error in the solution to the flow evolution equation (6), which demands that f_0 must be larger than 0.2 and f_1 larger than 0.5. Therefore, we examine models with $f_0 = 0.2\text{--}1.4$ and $f_1 = 0.5\text{--}3.0$, respectively, in intervals of 0.1. Each model group in Table 2 therefore includes 338 cases with different combinations of f_0 and f_1 .

3.1. TBL Thickness and CMB Heat Flow

[23] According to equation (6), the TBL thickness δ varies with time in proportion to f_0 and f_1 and is independent of ΔT and γ , so the time-averaged TBL thickness $\bar{\delta}$ and its standard deviation σ_δ depend only on f_0 and f_1 , which are shown in Figure 4a. The conductive heat flux can be calculated analytically as

$$q = -k \frac{dT}{dz} = \frac{2k\Delta T}{\sqrt{\pi}\delta} e^{-\left(\frac{z}{\delta}\right)^2}, \quad (22)$$

where k is the thermal conductivity. At the CMB $z = 0$, the heat flux is

$$q_{\text{CMB}} = \frac{2k\Delta T}{\sqrt{\pi}\delta}, \quad (23)$$

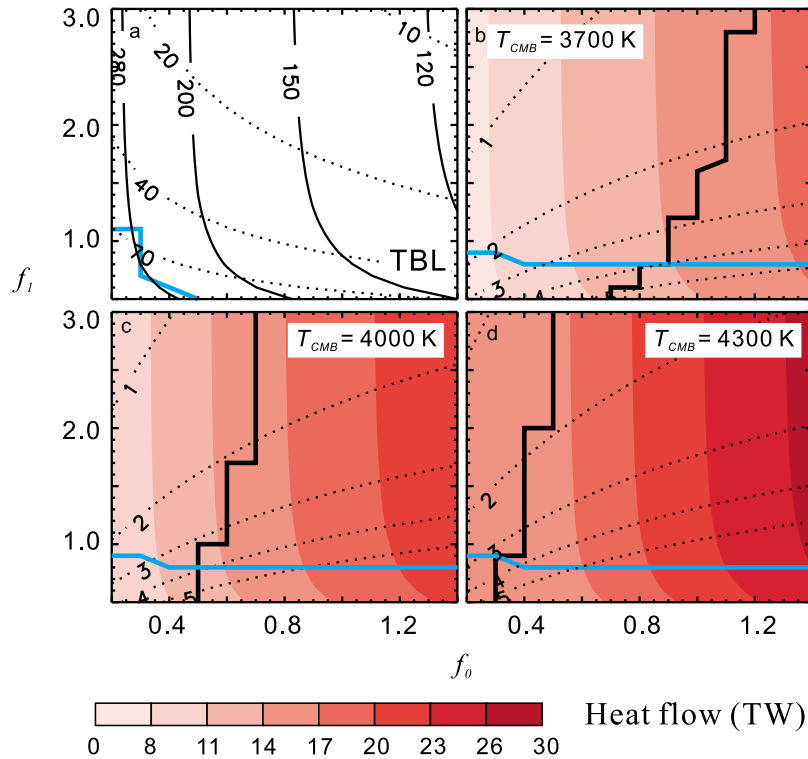


Figure 4. TBL thickness and CMB heat flow as a function of parameters f_0 and f_1 . (a) TBL thickness. Solid lines denote the time-averaged TBL thickness ($\bar{\delta}$); dotted lines denote the standard deviation (σ_δ). The region to the upper-right of the blue line corresponds to the seismically inferred height of $\bar{\delta} + \sigma_\delta \leq 400 \text{ km}$. (b–d) CMB heat flow contours for CMB temperatures of 3700, 4000, and 4300 K, respectively. Dotted lines indicate standard deviation of CMB heat flow (σ_Q). The region above the blue line corresponds to $\sigma_Q / \bar{Q}_{\text{CMB}} \leq 0.3$. The region to the left of the thick black line corresponds to $\bar{Q}_{\text{CMB}} + \sigma_Q \leq 18 \text{ TW}$.

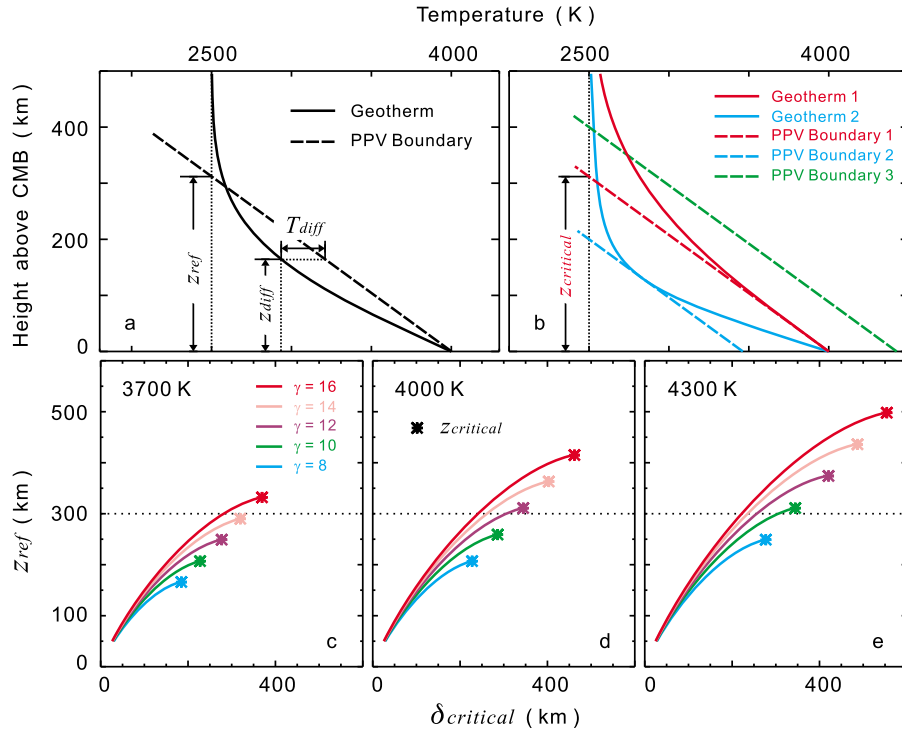


Figure 5. (a) Sketch of the PPV phase structure. (b) Three possible situations for the PPV phase transition. (c–e) Dependence of $\delta_{critical}$ on z_{ref} for CMB temperatures of 3700, 4000, 4300 K, respectively. The units of γ is MPa K $^{-1}$. Asterisks denote $z_{critical}$ for each combination of ΔT and γ . Dotted line indicates $z_{ref} = 300$ km.

and the total heat flow at the CMB is

$$Q_{CMB} = 4\pi R_{CMB}^2 q_{CMB} = \frac{8\sqrt{\pi}k\Delta TR_{CMB}^2}{\delta}, \quad (24)$$

which is only a function of ΔT and δ . Figures 4b–4d show the total CMB heat flow for different T_{CMB} from equation (24).

[24] From Figure 4a, f_0 and f_1 characterize the average and standard deviation of TBL thickness. δ is mostly sensitive to f_0 and increases with f_0 . In contrast, σ_δ decreases with f_1 . The quantity of $\delta \pm \sigma_\delta$ reaches a maximum of 402 ± 192 km at the bottom-left corner of Figure 4a and reaches a minimum of 115 ± 9 km at the top-right corner. To be consistent with seismic heterogeneity data, we restrict the maximum thickness of the TBL to $\delta + \sigma_\delta \leq 400$ km, which corresponds to the region to the right of the blue line. Hence, several cases at the lower-left corner in Figure 4a are not acceptable.

[25] The average thickness of the TBL is also constrained by energy considerations, because the CMB heat flow cannot be too small or too large. The time average of the CMB heat flow \bar{Q}_{CMB} , shown by red contours in Figures 4b–4d, is sensitive to f_0 and is also sensitive to the CMB temperature because of its dependence on ΔT . For the cases with a cold CMB of 3700 K, \bar{Q}_{CMB} ranges from 6 to 18 TW, while for the cases with a hot CMB of 4300 K and a thin TBL, \bar{Q}_{CMB} reaches 27 TW. Too low a CMB heat flow cannot maintain a convective dynamo in the outer core and too high a CMB heat flow is not compatible with surface heat flow constraints,

so we limit the minimum CMB heat flow $\bar{Q}_{CMB} - \sigma_Q$ to be greater than 4 TW and peak CMB heat flow $\bar{Q}_{CMB} + \sigma_Q$ to be less than 18 TW (corresponding to the area to the left of the thick black line in Figure 4), where σ_Q is the standard deviation of Q_{CMB} . For the cold CMB, about two thirds of the combinations of f_0 and f_1 are acceptable (Figure 4b), whereas for the warm CMB, only about one half of the cases are acceptable (Figure 4c). For the hot CMB, the acceptable area to the left of the black line amounts to less than 25% (Figure 4d). Adding the additional constraint based on dynamo modeling [Christensen and Olson, 2003] that σ_Q should be less than 30% of \bar{Q}_{CMB} , which corresponds to area above the blue line in Figures 4b–4d, then f_1 must be greater than 0.8 for most f_0 values.

3.2. PPV Phase Change Structure

[26] The equilibrium distribution of the PPV phase in the D'' layer is determined by the intersections of the PPV transition curve with the geotherm. The temperature of the PV–PPV phase transition boundary, T_{PPV} , can be obtained from equation (14) and the geotherm T from equation (5). We denote this temperature difference by T_{diff} , and z_{diff} is the corresponding height above the CMB. Figure 5a illustrates these relationships. According to equations (5) and (14),

$$T_{diff} = T - T_{PPV} = \Delta T \operatorname{erf}\left(\frac{z_{diff}}{\delta}\right) + \frac{\rho_m g}{\gamma}(z_{diff} - z_{ref}). \quad (25)$$

If T and T_{PPV} intersect at the CMB (red lines in Figure 5b), then $T_{diff} = 0$ at $z_{diff} = 0$, which gives a unique relationship

Table 3. PPV Phase Region Structure

Condition 1	Condition 2	PPV Structure in Depth	Condition 3	PPV Structure in Time
$z_{\text{ref}} \geq z_{\text{critical}}$	NA ^a	Single crossing	NA	PPV layer
$z_{\text{ref}} < z_{\text{critical}}$	$\delta \leq \delta_{\text{critical}}$	Double crossing	$\delta_{\text{top}} \leq \delta_{\text{critical}}$	PPV layer
	$\delta > \delta_{\text{critical}}$	No crossing (PPV absence)	$\delta_{\text{top}} > \delta_{\text{critical}}$	PPV lens
			$\delta_{\text{btm}} \leq \delta_{\text{critical}}$	
			$\delta_{\text{btm}} > \delta_{\text{critical}}$	No PPV

^aNot applicable.

between ΔT , γ , and z_{ref} . In this situation, z_{ref} has the critical value, defined as z_{critical} , given by

$$z_{\text{critical}} = \frac{\Delta T \gamma}{\rho_m g}, \quad (26)$$

which describes the case in which the single crossing occurs at the CMB.

[27] For a certain combination of ΔT and γ , if $z_{\text{ref}} > z_{\text{critical}}$, the PPV transition boundary (green dash line in Figure 5b) is above the geotherm near the CMB, and there must be PPV phase in the D'' region. In this situation, the PPV boundary crosses the geotherm only once in the lower mantle, which is the single-crossing structure. However, if $z_{\text{ref}} < z_{\text{critical}}$, the situation is more complicated. $T_{\text{diff_min}}$ donates to the minimum value of T_{diff} . $T_{\text{diff_min}} = 0$ means the PPV boundary (blue dash line in Figure 5b) is tangent to the geotherm (blue solid line in Figure 5b). If $T_{\text{diff_min}} > 0$, then PPV is absent, whereas if $T_{\text{diff_min}} < 0$, then the PPV transition boundary intersects geotherm twice, which is the structure known as the double-crossing structure.

[28] To find $T_{\text{diff_min}}$, we set the derivative of T_{diff} with respect to z_{diff} to 0:

$$\frac{dT_{\text{diff}}}{dz_{\text{diff}}} = -\frac{2\Delta T e^{-\left(\frac{z_{\text{diff}}}{\delta}\right)^2}}{\sqrt{\pi}\delta} + \frac{\rho_m g}{\gamma} = 0. \quad (27)$$

Solving equation (27) for z_{diff} yields

$$z_{\text{diff}} = \delta \sqrt{\ln\left(\frac{2\Delta T \gamma}{\rho_m g \sqrt{\pi}\delta}\right)}, \quad (28)$$

for the height at which T_{diff} reaches its minimum. Substituting equation (28) into equation (25),

$$T_{\text{diff_min}} = \Delta T \text{erfc}\left[\sqrt{\ln\left(\frac{2\Delta T \gamma}{\rho_m g \sqrt{\pi}\delta}\right)}\right] + \frac{\rho_m g}{\gamma} \left[\delta \sqrt{\ln\left(\frac{2\Delta T \gamma}{\rho_m g \sqrt{\pi}\delta}\right)} - z_{\text{ref}}\right]. \quad (29)$$

When $T_{\text{diff_min}} = 0$, we get the critical thickness of the TBL, denoted by δ_{critical} , determined by the requirement for the geotherm to contact the phase PPV boundary in the region where $z_{\text{ref}} < z_{\text{critical}}$. The dependence of δ_{critical} on z_{ref} is shown in Figures 5c–5e.

[29] In evaluating the TCP model, we have fixed the value of z_{ref} at 300 km. In groups of cases labeled as G3708, G3710, G3712, G3714, G4008, G4010, and G4308 (indicated by stars below the dotted line in Figures 5c–5e, respectively), $z_{\text{ref}} \geq z_{\text{critical}}$ so that there is a single crossing of

the phase boundary, where PPV is present most of the time. For the other eight groups of cases, the situations are diverse and the presence or absence of PPV depends on the detailed variation of the TBL. The conditions for PPV structures are summarized in Table 3.

[30] For each pair of f_0 and f_1 , the TBL thickness δ varies with time, as shown in Figure 3a. The minimum value of δ is denoted by δ_{btm} , and the maximum value by δ_{top} . In cases where $\delta_{\text{top}} \leq \delta_{\text{critical}}$, which means $\delta \leq \delta_{\text{critical}}$ for all time, the PPV phase forms a layer in the D'' region. Alternatively, in some cases where $\delta_{\text{top}} > \delta_{\text{critical}}$ but $\delta_{\text{btm}} \leq \delta_{\text{critical}}$, the PPV is present only for a limited time, the situation that corresponds to a PPV lens (Figure 3c). However, in cases where $\delta_{\text{btm}} > \delta_{\text{critical}}$ for all time, there is no PPV at all. The value of δ_{critical} at $z_{\text{ref}} = 300$ km is shown in Figure 6a. The maximum δ_{btm} for all f_0 and f_1 is 224.0 km, obtained at $f_0 = 0.2$ and $f_1 = 3.0$, and it is larger than the $\delta_{\text{critical}} = 221.8$ km of G4316. Therefore, the PPV phase is absent in case C4316_0230, and case C4316_0229 with $\delta_{\text{btm}} = 222.4$ km. All other cases in G4316 have either PPV lenses or layers. Figure 6b shows the conditions for which a PPV lens or PPV layer is present for the cases in eight groups with $z_{\text{ref}} < z_{\text{critical}}$. The other seven groups with single-phase boundary crossings have a continuous PPV layer.

3.3. Seismic Shear Wave Velocity Variations

[31] The most quantitative constraints on the boundary layer structure in the D'' region comes from the lateral variation of seismic velocities in the lowermost mantle. Figure 7a shows the root mean square (RMS) variation of V_S in the lowermost mantle from seismic tomography: SAW642AN, S20RTS, PRI-S05, TX2008J, and SMEAN. To compare these profiles with the TCP model cases, we define a fitting area for V_S heterogeneity (shaded region in Figure 7a) from 50 to 300 km above the CMB, which corresponds to the boundary layer portion of D'' . The RMS variation of the synthetic $d \ln V_S$ from the TCP model using equation (18) is defined as

$$\sigma_V(z) = \sqrt{(d \ln V_S)^2} = \sqrt{\frac{1}{\tau} \int_0^\tau (d \ln V_S)^2 dt}, \quad (30)$$

which is a function of height above the CMB.

[32] The TCP model cases that produce $d \ln V_S$ variations similar to those observed are considered acceptable and can be used to constrain physical properties of the D'' region. To assess the fit, we adopt the following success criteria: (1) In all, 85% of the σ_V profile fits in the fitting area or better. (2) A total of 45% of the σ_V profile has increasing trend from top of D'' to the CMB. (3) The maximum value of the σ_V

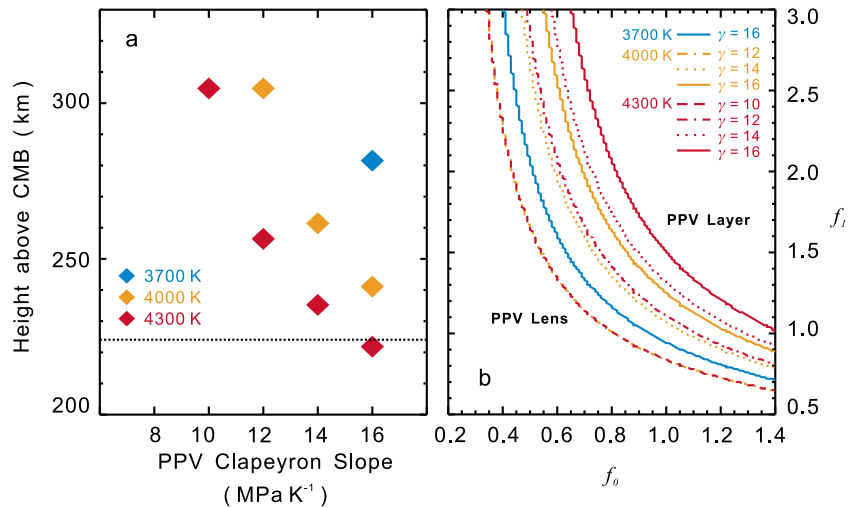


Figure 6. (a) The δ_{critical} versus PPV Clapeyron slope for $z_{\text{ref}} = 300$ km. Dashed line is the maximum δ_{btm} for all TCP model cases. (b) PPV phase region structure as a function of f_1 and f_0 for various values of γ in MPa K^{-1} . The cases to the left of the curves have PPV lens, whereas the cases to the right have PPV layer.

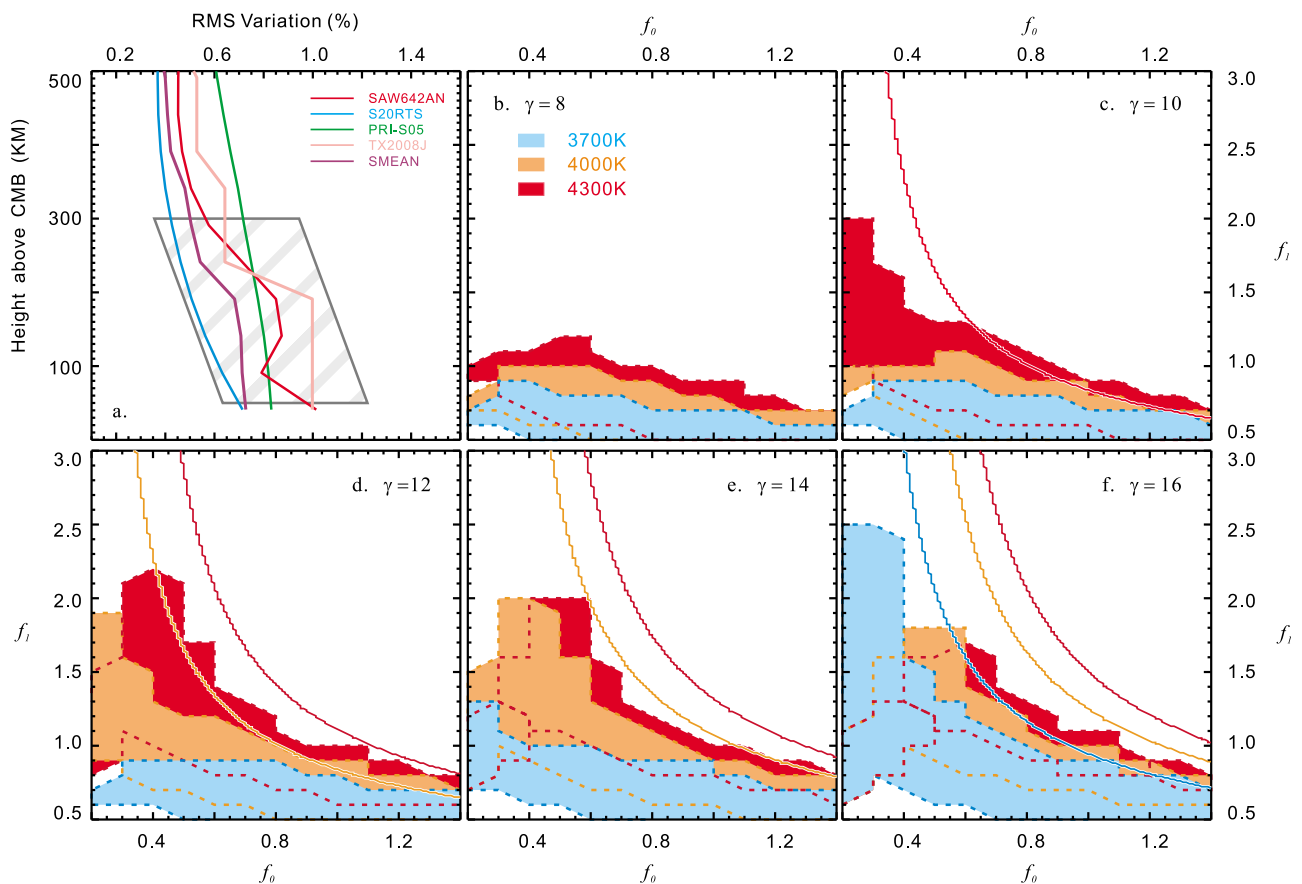


Figure 7. (a) RMS variation of shear wave velocity anomaly from four seismic tomography models. Shaded region is the acceptable area for the TCP model cases. (b–f) The range of acceptable TCP model cases according to the σ_V profile criteria in Table 4. The units of γ is MPa K^{-1} . Solid lines separate regions with PPV lens and layer structures (same as in Figure 6b).

Table 4. Criteria of TCP Model Case Selection

	Property	Acceptable Criteria	Best-Fitting Criteria
σ_V Profile	Fitting percentage	$\geq 85\%$	$\geq 85\%$
	Increasing trend	$\geq 45\%$	$\geq 65\%$
$d\ln V_S$ Distribution	Location for maximum	≤ 200 km	≤ 100 km
	Correlation to Gaussian	≥ 0.90	≥ 0.95
	Equivalent width	≥ 1.5	≥ 2.0
	Skewness	NA ^a	Negative tail
CMB Heat Flow		$\bar{Q}_{CMB} + \sigma_Q \leq 18\text{TW}$	$\bar{Q}_{CMB} + \sigma_Q \leq 18\text{TW}$
		NA	$\sigma_Q / \bar{Q}_{CMB} \leq 0.3$

^aNot applicable.

profile is located within 200 km above the CMB. The cases that meet these criteria are shown in Figures 7b–7f. Most of the successful cases are to the left of the separator lines, which demonstrate the importance of PPV lenses on the V_S heterogeneity. In addition, cases toward the bottom-left corner in Figure 7 have large σ_δ , which results in large lateral variation in temperature; these have too large V_S heterogeneity to match the observations in the fitting area.

3.4. Statistical Properties of the Best Fitting Cases

[33] Constraints used to identify the best TCP models include the σ_V profile and CMB heat flow estimates, which have been described previously. In addition, the synthetic $d\ln V_S$ distribution should be Gaussian-like. We adopt the following criteria for the $d\ln V_S$ distribution for the best fitting cases: (1) the correlation of the $d\ln V_S$ distribution with a Gaussian distribution is greater than 0.95; (2) the equivalent width of the $d\ln V_S$ distribution is greater than 2; and

(3) there is skewness of the $d\ln V_S$ distribution with a negative tail. These constraints are summarized in Table 4, yielding six criteria for acceptable cases and eight criteria for best fitting cases. Ten TCP model groups G3714, G3716, G4010, G4012, G4014, G4016, G4310, G4312, G4314, and G4316 yielded acceptable cases (blue squares in Figure 8), whereas only G4014 yielded best fitting cases (red squares in Figure 8), corresponding to $f_0 = 0.5$ –0.6 and $f_1 = 0.9$ –1.5.

[34] For nominal values of $T_{CMB} = 4000$ K and $\gamma = 14$ MPa K⁻¹, case C4014_0511 is an example of the best fitting cases with $f_0 = 0.5$ and $f_1 = 1.1$. In case C4014_0511, the variances of temperature, composition (iron enrichment), and PPV phase anomalies $\overline{T'^2}$, $\overline{\chi'_{Fe}^2}$, and $\overline{\varphi'_{PPV}^2}$ from equations (8), (13), and (17) are shown as RMS variations in Figures 9a–9c, respectively. In Figure 9d, the RMS variation of the synthetic $d\ln V_S$ gives a good fit to the lower mantle seismic tomography in the middle portion of D'' , from about

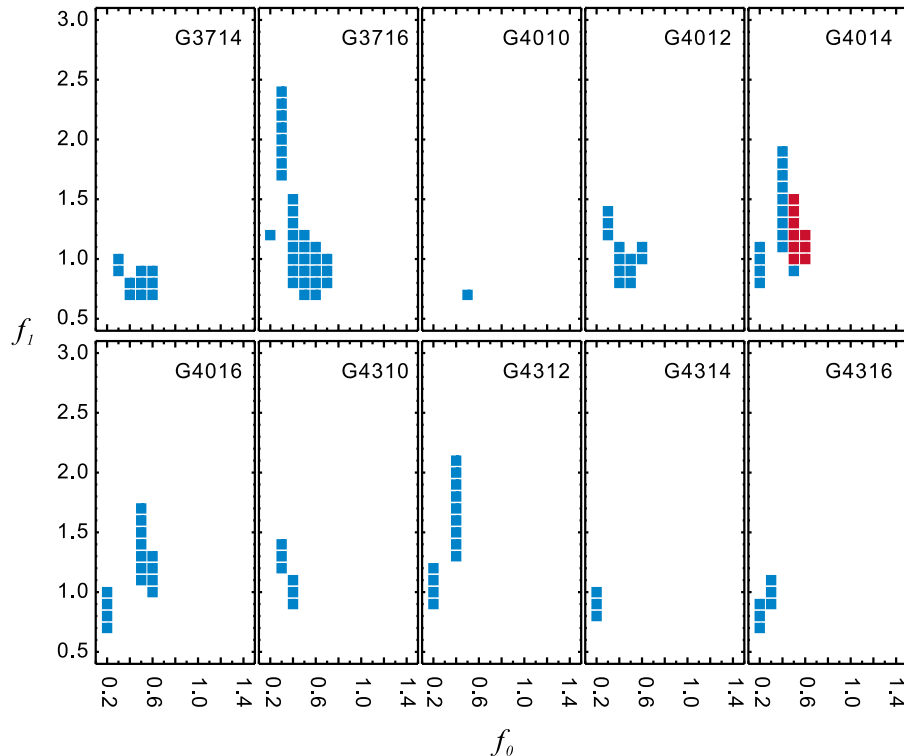


Figure 8. Acceptable TCP model cases (blue) and best fitting cases (red) according to the criteria in Table 4.

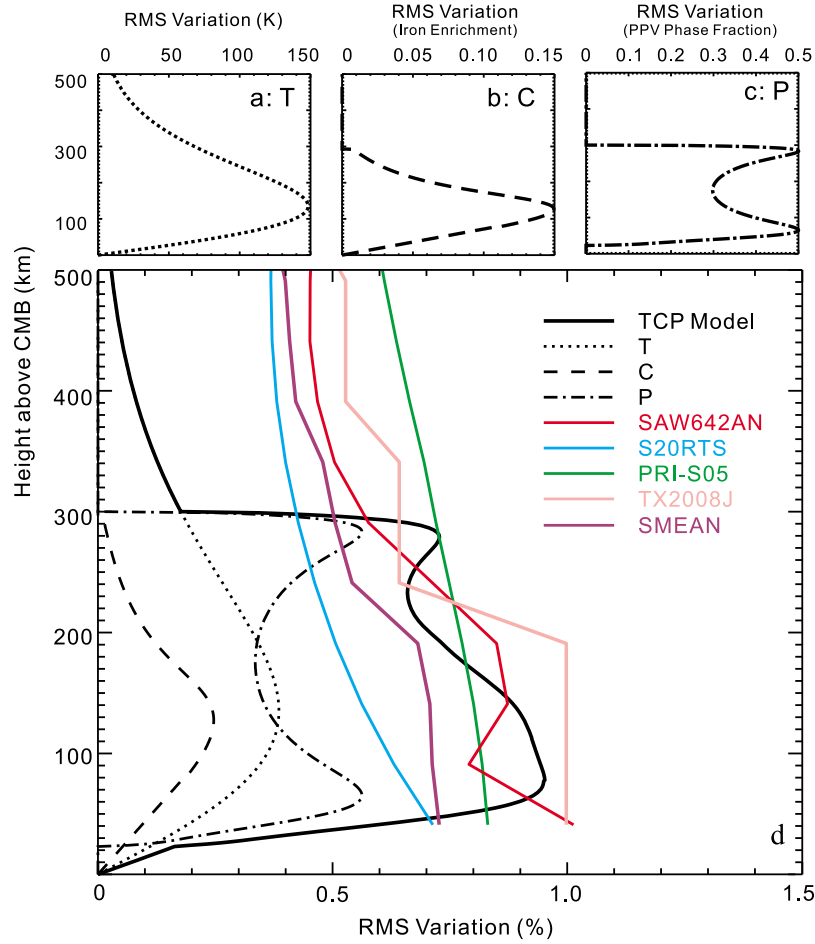


Figure 9. Statistical properties of the best fitting TCP model case C4014_0511. (a–c) RMS variations for temperature, composition, and PPV phase anomalies, respectively. (d) RMS variations of seismic shear wave velocity anomaly from the TCP model (black line) and seismic tomography (colored lines). The individual contributions to seismic velocity heterogeneity from temperature (T), composition (C), and PPV phase (P) are also shown.

50 km to about 300 km above the CMB. We defined the misfit M as

$$M = \frac{1}{220} \int_{70}^{290} \frac{(\sigma_V(z) - \sigma_{V^*}(z))^2}{\sigma_{V^*}(z)^2} dz, \quad (31)$$

where σ_{V^*} is the RMS variation of observed V_S . The misfits of synthetic V_S to seismic tomography models SAW642AN, S20RTS, PRI-S05, TX2008J, and SMEAN are 1.4%, 25%, 1.1%, 1.9%, and 6.6%, respectively. However, the fit degrades, at the two jumps in Figure 9, for example, in the regions above 300 km and below 50 km. The region above 300 km is probably outside the D'' layer and outside the TCP model domain of validity, so a large misfit with the data is expected. The region below 50 km is too close to the CMB for most global seismic tomography to resolve heterogeneity, and in this region, there may also be partial melting, which is not included in the TCP model calculation.

[35] Figure 9d also shows that the thermal heterogeneity is maximum around 150 km above the CMB and accounts for slightly less than 50% of the seismic heterogeneity there (dot line in Figure 9d). Chemically produced heterogeneity has

nearly the same distribution with depth as thermal heterogeneity but with less than half of the amplitude (dash line in Figure 9d). Heterogeneity due to the PPV phase change (dot-dash line in Figure 9d) has a bimodal profile, with maxima near 300 km and 70 km above the CMB, respectively, corresponding to a double-crossing structure for this phase change, and accounts for more than 50% of the overall seismic heterogeneity.

[36] The best fitting case C4014_0511 has a TBL thickness of about 205 ± 45 km (Figure 3a), which is close to the observed thickness of the D'' layer of approximately 250 km. The CBL for this case has a similar structure to the TBL, with a thickness of 154 ± 35 km (Figure 3b). The PPV lens ranges from 20 to 300 km above the CMB (Figure 3c), which is comparable with the average location of the seismic discontinuity [Wysession *et al.*, 1998].

3.5. Correlation of CMB Heat Flux and S Wave Velocity in the D'' Region

[37] The anomaly of CMB heat flux q_{CMB} is defined as

$$d \ln q_{\text{CMB}} = \frac{q_{\text{CMB}} - \bar{q}_{\text{CMB}}}{\bar{q}_{\text{CMB}}}, \quad (32)$$

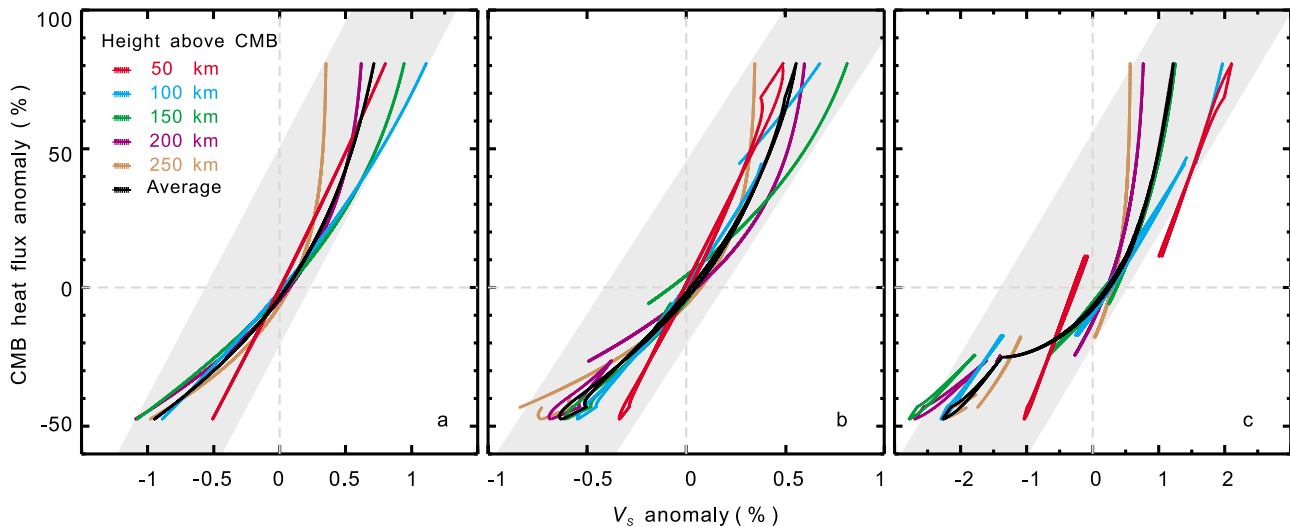


Figure 10. Correlation of D'' seismic shear wave heterogeneity and relative CMB heat flux anomalies from the case C4014_0511. Colored curves indicate the correlation with V_S anomaly at different heights above the CMB, respectively. Black curve is the correlation with the V_S anomaly averaged from 50 to 300 km. Shaded areas indicate the fitting regions. (a) The V_S anomaly is due to temperature only. The slope of the fitting area is +90. (b) The V_S anomaly is due to both temperature and composition, and the fitting region slope is +110. (c) The V_S anomaly includes thermal, compositional, and PPV phase contributions. The fitting region slope is approximately +40.

where \bar{q}_{CMB} is the time average of the CMB heat flux. The correlation between $d\ln q_{\text{CMB}}$ and the synthetic $d\ln V_S$ of case C4014_0511 shown in Figure 10 is positive. Comparing Figures 10a and 10b, chemical heterogeneity slightly increases the slope of the correlations from 90 to 110, while the PPV phase transition further complicates this correlation (Figure 10c). The existence of the PPV phase tends to break the correlation into discrete segments, although it remains linear within each segment. These results are comparable to those found by Nakagawa and Tackley [2008] using a 3-D mantle convection model.

4. Discussion

[38] It is generally accepted that heat transfer from the core to the mantle governs the dynamics in the D'' region above the CMB, although both the average and the spatial variation of the CMB heat flow remain highly uncertain. A variety of techniques have been used to place constraints on these properties. For examples, Buffett [2007] considered the D'' flow driven by the negative buoyancy of the PPV phase and to estimate a lower bound on the local CMB heat flux, and Hernlund [2010] estimated the CMB heat flow beneath a PPV lens formed near the base of a downwelling region in the lower mantle. Our study attempts to constrain the global variations of CMB heat flow to provide a statistical characterization of the thermal regime applicable to the entire CMB.

[39] According to our analytical and numerical results, lateral temperature variations are the most important factor controlling the seismic heterogeneity in the D'' region. The central portion of the $d\ln V_S$ distribution is produced by temperature heterogeneity, according to Figure 2f. However, the depth dependence of the RMS $d\ln V_S$ in D'' cannot be explained by a heterogeneous thermal boundary layer alone.

[40] The presence of chemical heterogeneity in the lowermost mantle has been argued from multiple perspectives [e.g., Deschamps and Trampert, 2003; Hofmann, 1997; Ishii and Tromp, 1999, 2004]. In the TCP model, the chemical contributions to the V_S heterogeneity, in particular, the D'' material with anomalously high iron content, produce a tail with a smaller peak around -1.6% in the negative portion of the distribution. A similar explanation of this skewness has been given by Hernlund and Houser [2008], who proposed a bimodal distribution. Note that this implies that the heterogeneity of chemical variation needs to be smaller than that of thermal variation for the central lobe in the statistical distribution to remain Gaussian-like.

[41] In addition, the PPV phase transitions contribute strong heterogeneity in the D'' region. The large negative V_S anomalies that skew the distribution and produce the long negative tail (Figure 2) may be interpreted as an effect of the PPV phase change, as previously proposed by Hernlund and Houser [2008]. The PPV phase changes with a double-crossing structure generate heterogeneity concentrated near the phase transition boundaries (dot-dash-line in Figure 9), which increases the RMS $d\ln V_S$ variation at several tens of kilometers above the CMB, especially at the height of the second crossing where there is a jump from 0.5% to 1% of RMS in the model. Without the contribution from PPV lenses, the RMS variation of the synthetic $d\ln V_S$ tends to be smaller than what is observed.

[42] With the assumed lower mantle temperature of 2500 K, to produce PPV lenses, certain combinations of CMB temperature and PPV Clapeyron slope are necessary. The CMB temperature is currently estimated to lie within the range of 3700–4400 K [Boehler, 2000; Steinberger and Holme, 2008; van der Hilst et al., 2007], although the actual uncertainty might be larger. We find that a combination of factors favor a CMB temperature near 4000 K,

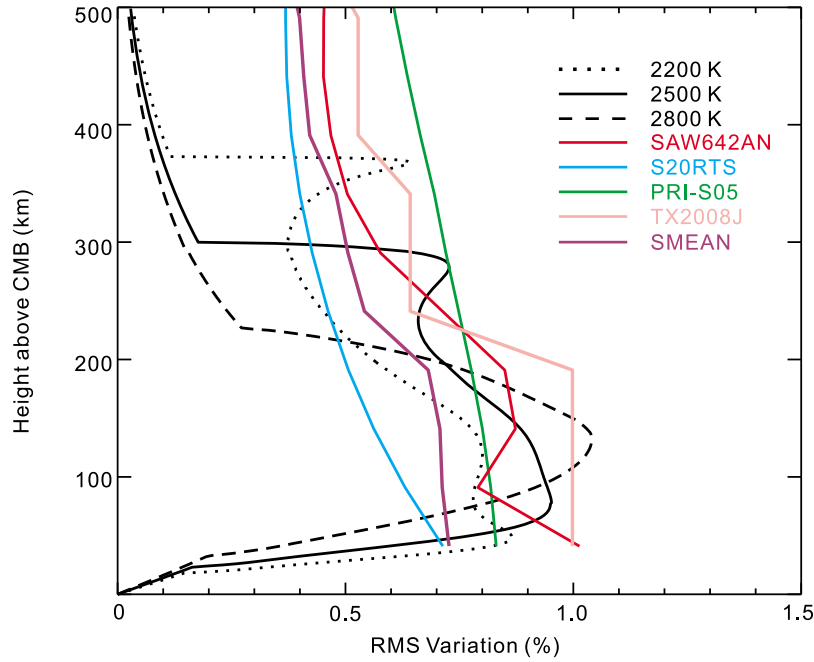


Figure 11. RMS lateral variations of seismic S wave velocity from the TCP models with different lower mantle temperatures of 2200, 2500, and 2800 K, respectively. Colored lines are seismic tomography models.

comparable to previous estimates based on the melting temperature of iron [Boehler, 1993]. In contrast, too high a CMB temperature yields unrealistically large CMB heat flow (Figure 4d), and CMB temperatures of 3700 K or lower require a very large Clapeyron slope, even larger than 16 MPa K^{-1} , to produce double-crossing phase transitions.

[43] However, the variation of the lower mantle temperature also impacts the PPV structure. To examine the sensitivity to variations in lower mantle temperature, we changed the lower mantle temperature to 2200 and 2800 K in the best fitting model case C4014_0511. A lower mantle temperature of 2200 K has the effect of increasing the thickness of PPV lenses, as shown by the dotted line in Figure 11, while an increase in the lower mantle temperature to 2800 K results in PPV lenses that are much thinner and smaller in volume, as shown by the dashed line in Figure 11.

[44] High-pressure measurements and mineral structure calculations offer support for a positive Clapeyron slope for the PPV phase transformation [Oganov and Ono, 2004; Tsuchiya et al., 2004], but there is little agreement on its magnitude. In the TCP model, a limited range of Clapeyron slopes γ produces PPV lenses with reasonable CMB temperatures. Too small γ generates a phase structure with single crossings instead of double crossings, whereas too large γ eliminates the PPV phase entirely (i.e., no crossings), especially in cases with low CMB temperature. In contrast, with a hotter CMB temperature, the Clapeyron slope could be smaller. In Figure 8, the best fitting cases with $T_{\text{CMB}} = 4000 \text{ K}$ yield $\gamma = +14 \text{ MPa K}^{-1}$ and $z_{\text{ref}} = 300 \text{ km}$, which is comparable with Tateno et al. [2009].

[45] An alternative way to specify the location of the PPV phase is to use as a reference the temperature of the phase transition at the CMB pressure, T_{int} , a technique used by

Hernlund et al. [2005] and Monnereau and Yuen [2007, 2010]. To compare our results with theirs, we introduced T_{int} defined as

$$T_{\text{int}} = T_{\text{ref}} + \frac{\rho_m g}{\gamma} z_{\text{ref}}. \quad (33)$$

In terms of this parameter, the requirement of single crossing according to equation (26) can now be expressed as $T_{\text{int}} \geq T_{\text{CMB}}$, which is equivalent to the definition used by Hernlund et al. [2005] and Monnereau and Yuen [2007, 2010]. In addition, in the best fitting model case C4014_0511, we obtain $T_{\text{int}} = 3738 \text{ K}$, different from T_{CMB} , by only 262 K, which is very close to the difference of 200 K of Monnereau and Yuen [2007, 2010].

[46] Recent studies estimate CMB heat flow in the range of 6–17 TW [Labrosse, 2002; Lay et al., 2006; Tateno et al., 2009; van der Hilst et al., 2007]. In case C4014_0511, the CMB heat flow is $13 \pm 3 \text{ TW}$ (Figure 4b), which is close to the current estimates of the mean and variation [Lay et al., 2006]. We can also calculate the plume heat flux, assuming that the plume is thin and draws its heat from the material above the CBL. Then the plume heat flux is given by

$$Q_{\text{plume}} = 4\pi R_{\text{CMB}}^2 \Delta T \rho_m C_p f \int_h^\infty \text{erfc}\left(\frac{z}{\delta(t)}\right) dz. \quad (34)$$

The time-average plume flux of the case C4014_0511 is approximately 3 TW, within the range of 2–4 TW obtained by Davies [1988] and Sleep [1990] from hot spot swells.

[47] The TCP boundary layer model simulates dynamics of mantle flow in the D'' region away from energetic regions

such as plume generation zones (PGZs) and subducted slabs. However, it can be compared to global seismic tomography statistics, because these energetic regions only occupy relatively small areas of the CMB [Becker and Boschi, 2002; Kuo et al., 2000; Steinberger, 2000]. Burke et al. [2008] suggested that PGZs are narrow horizontal belts that straddle the -1% $d\ln V_S$ contour in the tomographic model by Becker and Boschi [2002]. They also suggested that cold former slab material sinking toward the CMB corresponds to the fast S wave velocity in D'' . Although the TCP model fails to describe the motion directly beneath plumes and slabs, it is applicable to the margins of these structures. As seen in Figure 2, the statistical distribution of the synthetic $d\ln V_S$ does not have the straddle between -1% and -1.6% nor the positive portion larger than 1.1% that is evident in the tomographic data. In addition, we tested the impact of plumes and slabs on the RMS variation of $d\ln V_S$, which is small and can be negligible.

[48] Chemical dynamics is probably complex in the D'' layer, with sinking slab and iron diffusing into and out of the core being examples. Iron heterogeneity is perhaps the most important on the dynamics of the flow by virtue of its large density contrast. Mao et al. [2004] proposed that the PPV phase with higher iron content may be stable at higher temperatures. Furthermore, some thermodynamic properties of the PPV phase may also be important to change the dynamics of the boundary layer. For instance, the thermal conductivity of the PPV may be as much as 50% higher than the PV [Ohta et al., 2008]. In addition, Ammann et al. [2010] have proposed that the viscosity of the PPV is significantly lower than the PV. Therefore, future extensions of this approach may include the effects of PPV phase dynamics, due to the variation of iron content, the influence of melting, and the contrast in physical properties between PV and PPV, along with the constraints from seismic anisotropy [Miyagi et al., 2010].

[49] In this article, the main seismological constraint is from shear wave velocity, but we did not consider the bulk sound speed heterogeneity. The P wave heterogeneity in D'' layer is weak, and its variation is less well characterized, although Wookey et al. [2005] interpreted a very weak P wave reflection due to PPV. Future extensions of the TCP model might focus on the origin of the anticorrelation of shear wave velocity and bulk sound velocity in the D'' region [Masters et al., 2000]. Another missing piece is the lowermost 100 km of the mantle, which is lacking in global coverage of its seismic heterogeneity; this region may contain important properties that could further constrain the interpretation of the main D'' structure.

5. Conclusions

[50] The fundamental assumption in the TCP boundary layer model is the statistical equivalence between temporal and spatial variations of temperature and composition in the D'' region. On the basis of this equivalence, we used a time history in the TCP boundary layer model that is predicated on a cycle of thermochemical pile growth and collapse, deep subduction, and plume formation events to produce seismic S wave velocity variations in time that are comparable to the observed statistics of the present-day spatial heterogeneity of shear wave velocity in the D'' region.

[51] We find that the increase in seismic S wave velocity heterogeneity observed in the D'' region compared to the rest of the lower mantle can be explained by the combined effects of a 1500 K radial temperature change, a chemically dense layer with an approximately 150 km average thickness, and PPV lenses in the heterogeneous boundary layer. The TCP model case C4014_0511 predicts CMB heat flow in the range of 13 ± 3 TW and a deep mantle plume heat flux of approximately 3 TW. The boundary layer model predicts an almost linear correlation between seismic S wave velocity anomalies in the D'' region and CMB heat flow anomalies, except where PPV lenses are present.

[52] **Acknowledgments.** This research is supported by grant EAR-0909622 from the NSF Geophysics Program. We thank M. Monnereau and an anonymous reviewer for their helpful comments.

References

- Ammann, M. W., J. P. Brodholt, J. Wookey, and D. P. Dobson (2010), First-principles constraints on diffusion in lower-mantle minerals and a weak D'' layer, *Nature*, *465*, 462–465, doi:10.1038/nature09052.
- Becker, T. W., and L. Boschi (2002), A comparison of tomographic and geodynamic mantle models, *Geochem. Geophys. Geosyst.*, *3*, 1003, doi:10.1029/2001GC000168.
- Boehler, R. (1993), Temperatures in the Earth's core from melting-point measurements of iron at high static pressures, *Nature*, *363*, 534–536, doi:10.1038/363534a0.
- Boehler, R. (1996), Melting temperature of the Earth's mantle and core: Earth's thermal structure, *Annu. Rev. Earth Planet. Sci.*, *24*, 15–40, doi:10.1146/annurev.earth.24.1.15.
- Boehler, R. (2000), High-pressure experiments and the phase diagram of lower mantle and core materials, *Rev. Geophys.*, *38*, 221–245, doi:10.1029/1998RG000053.
- Buffett, B. A. (2002), Estimates of heat flow in the deep mantle based on the power requirements for the geodynamo, *Geophys. Res. Lett.*, *29*(12), 1566, doi:10.1029/2001GL014649.
- Buffett, B. A. (2003), The thermal state of Earth's core, *Science*, *299*, 1675–1677, doi:10.1126/science.1081518.
- Buffett, B. A. (2007), A bound on heat flow below a double crossing of the perovskite-postperovskite phase transition, *Geophys. Res. Lett.*, *34*, L17302, doi:10.1029/2007GL030930.
- Bullen, K. E. (1949), Compressibility-pressure hypothesis and the Earth's interior, *Geophys. J. Int.*, *5*, 335–368, doi:10.1111/j.1365-246X.1949.tb02952.x.
- Burke, K., and T. H. Torsvik (2004), Derivation of large igneous provinces of the past 200 million years from long-term heterogeneities in the deep mantle, *Earth Planet. Sci. Lett.*, *227*, 531–538, doi:10.1016/j.epsl.2004.09.015.
- Burke, K., B. Steinberger, T. H. Torsvik, and M. A. Smethurst (2008), Plume generation zones at the margins of large low shear velocity provinces on the core-mantle boundary, *Earth Planet. Sci. Lett.*, *265*, 49–60, doi:10.1016/j.epsl.2007.09.042.
- Christensen, U. R., and P. Olson (2003), Secular variation in numerical geodynamo models with lateral variations of boundary heat flow, *Phys. Earth Planet. Inter.*, *138*, 39–54, doi:10.1016/S0031-9201(03)00064-5.
- Courtillot, V., and P. Olson (2007), Mantle plumes link magnetic superchrons to Phanerozoic mass depletion events, *Earth Planet. Sci. Lett.*, *260*, 495–504, doi:10.1016/j.epsl.2007.06.003.
- Davies, G. F. (1988), Ocean bathymetry and mantle convection: 1. Large-scale flow and hotspots, *J. Geophys. Res.*, *93*, 10,467–10,480, doi:10.1029/JB093iB09p10467.
- Deschamps, F., and J. Trampert (2003), Mantle tomography and its relation to temperature and composition, *Phys. Earth Planet. Inter.*, *140*, 277–291, doi:10.1016/j.pepi.2003.09.004.
- Deschamps, F., and J. Trampert (2004), Towards a lower mantle reference temperature and composition, *Earth Planet. Sci. Lett.*, *222*, 161–175, doi:10.1016/j.epsl.2004.02.024.
- Deschamps, F., J. Trampert, and P. J. Tackley (2007), Thermo-chemical structure of the lower mantle: Seismological evidence and consequences for geodynamics, in *Superplumes: Beyond Plate Tectonics*, edited by D. A. Yuen et al., pp. 293–320, Springer, Netherlands, doi:10.1007/978-1-4020-5750-2_11.
- Garnero, E. J. (2000), Heterogeneity of the lowermost mantle, *Annu. Rev. Earth Planet. Sci.*, *28*, 509–537, doi:10.1146/annurev.earth.28.1.509.

- Garnero, E. J., and D. V. Helmberger (1996), Seismic detection of a thin laterally varying boundary layer at the base of the mantle beneath the central-Pacific, *Geophys. Res. Lett.*, *23*, 977–980, doi:10.1029/95GL03603.
- Hansen, U., and D. A. Yuen (1988), Numerical simulations of thermal-chemical instabilities at the core-mantle boundary, *Nature*, *334*, 237–240, doi:10.1038/334237a0.
- Hernlund, J. W. (2010), On the interaction of the geotherm with a post-perovskite phase transition in the deep mantle, *Phys. Earth Planet. Inter.*, *180*, 222–234, doi:10.1016/j.pepi.2010.02.001.
- Hernlund, J. W., and C. Houser (2008), The statistical distribution of seismic velocities in Earth's deep mantle, *Earth Planet. Sci. Lett.*, *265*, 423–437, doi:10.1016/j.epsl.2007.10.042.
- Hernlund, J. W., C. Thomas, and P. J. Tackley (2005), A doubling of the post-perovskite phase boundary and structure of the Earth's lowermost mantle, *Nature*, *434*, 882–886, doi:10.1038/nature03472.
- Hofmann, A. W. (1997), Mantle geochemistry: The message from oceanic volcanism, *Nature*, *385*, 219–229, doi:10.1038/385219a0.
- Howard, L. N. (1964), Convection at high Rayleigh numbers, in *Applied Mechanics, Proceedings of the 11th Congress of Applied Mathematics*, edited by H. Gortler, pp. 1109–1115, Springer, Berlin.
- Hutko, A. R., T. Lay, E. J. Garnero, and J. Revenaugh (2006), Seismic detection of folded, subducted lithosphere at the core-mantle boundary, *Nature*, *441*, 333–336, doi:10.1038/nature04757.
- Hutko, A. R., T. Lay, J. Revenaugh, and E. J. Garnero (2008), Anticorrelated seismic velocity anomalies from post-perovskite in the lowermost mantle, *Science*, *320*, 1070–1074, doi:10.1126/science.1155822.
- Ishii, M., and J. Tromp (1999), Normal-mode and free-air gravity constraints on lateral variations in velocity and density of Earth's mantle, *Science*, *285*, 1231–1236, doi:10.1126/science.285.5431.1231.
- Ishii, M., and J. Tromp (2004), Constraining large-scale mantle heterogeneity using mantle and inner-core sensitive normal modes, *Phys. Earth Planet. Inter.*, *146*, 113–124, doi:10.1016/j.pepi.2003.06.012.
- Jaupart, C., S. Labrosse, and J.-C. Mareschal (2007), Temperatures, heat and energy in the mantle of the Earth, in *Treatise on Geophysics*, vol. 7, edited by G. Schubert, pp. 253–304, Elsevier, New York, doi:10.1016/B978-044452748-6.00114-0.
- Knittle, E., and R. Jeanloz (1991), Earth's core-mantle boundary: Results of experiments at high pressures and temperatures, *Science*, *251*, 1438–1443, doi:10.1126/science.251.5000.1438.
- Kumagai, I., A. Davaille, K. Kurita, and E. Stutzmann (2008), Mantle plumes: Thin, fat, successful, or failing? Constraints to explain hot spot volcanism through time and space, *Geophys. Res. Lett.*, *35*, L16301, doi:10.1029/2008GL035079.
- Kuo, B. Y., E. J. Garnero, and T. Lay (2000), Tomographic inversion of S-SKS times for shear velocity heterogeneity in D'' : Degree 12 and hybrid models, *J. Geophys. Res.*, *105*, 28,139–28,157, doi:10.1029/2000JB900334.
- Labrosse, S. (2002), Hotspots, mantle plumes and core heat loss, *Earth Planet. Sci. Lett.*, *199*, 147–156, doi:10.1016/S0012-821X(02)00537-X.
- Labrosse, S., J. P. Poirier, and J. L. Le Mouél (2001), The age of the inner core, *Earth Planet. Sci. Lett.*, *190*, 111–123, doi:10.1016/S0012-821X(01)00387-9.
- Lay, T., and E. J. Garnero (2004), Core-mantle boundary structures and processes, in *State of the Planet: Frontiers and Challenges in Geophysics*, edited by R. S. J. Sparks and C. J. Hawkesworth, pp. 25–41, AGU, Washington, D. C., doi:10.1029/150GM04.
- Lay, T., and D. V. Helmberger (1983), A shear velocity discontinuity in the lower mantle, *Geophys. Res. Lett.*, *10*, 63–66, doi:10.1029/GL010i001p00063.
- Lay, T., Q. Williams, and E. J. Garnero (1998), The core-mantle boundary layer and deep Earth dynamics, *Nature*, *392*, 461–468, doi:10.1038/33083.
- Lay, T., E. J. Garnero, and Q. Williams (2004), Partial melting in a thermochemical boundary layer at the base of the mantle, *Phys. Earth Planet. Inter.*, *146*, 441–467, doi:10.1016/j.pepi.2004.04.004.
- Lay, T., J. Hernlund, E. J. Garnero, and M. S. Thorne (2006), A post-perovskite lens and D'' heat flux beneath the central Pacific, *Science*, *314*, 1272–1276.
- Lay, T., J. Hernlund, and B. A. Buffett (2008), Core-mantle boundary heat flow, *Nat. Geosci.*, *1*, 25–32, doi:10.1038/ngeo.2007.44.
- Mao, W. L., G. Y. Shen, V. B. Prakapenka, Y. Meng, A. J. Campbell, D. L. Heinz, J. F. Shu, R. J. Hemley, and H. K. Mao (2004), Ferromagnesian postperovskite silicates in the D'' layer of the Earth, *Proc. Natl. Acad. Sci. U. S. A.*, *101*, 15,867–15,869.
- Maruyama, S., M. Santosh, and D. Zhao (2007), Superplume, supercontinent, and post-perovskite: Mantle dynamics and anti-plate tectonics on the core-mantle boundary, *Gondwana Res.*, *11*, 7–37, doi:10.1016/j.gr.2006.06.003.
- Masters, G., G. Laske, H. Bolton, and A. Dziewonski (2000), The relative behavior of shear velocity, bulk sound speed, and compressional velocity in the mantle: Implications for chemical and thermal structure, in *Earth's Deep Interior, Geophys. Monogr. Ser.*, vol. 117, pp. 63–87, AGU, Washington, D. C.
- McNamara, A. K., and S. J. Zhong (2005), Thermochemical structures beneath Africa and the Pacific Ocean, *Nature*, *437*, 1136–1139, doi:10.1038/nature04066.
- Miyagi, L., W. Kanitpanyacharoen, P. Kaercher, K. K. M. Lee, and H. R. Wenk (2010), Slip systems in MgSiO_3 post-perovskite: Implications for D'' anisotropy, *Science*, *329*, 1639–1641, doi:10.1126/science.1192465.
- Monnereau, M., and D. A. Yuen (2007), Topology of the postperovskite phase transition and mantle dynamics, *Proc. Natl. Acad. Sci. U. S. A.*, *104*, 9156–9161, doi:10.1073/pnas.0608480104.
- Monnereau, M., and D. A. Yuen (2010), Seismic imaging of the D'' and constraints on the core heat flux, *Phys. Earth Planet. Inter.*, *180*, 258–270, doi:10.1016/j.pepi.2009.12.005.
- Montelli, R., G. Nolet, F. A. Dahlen, and G. Masters (2006), A catalogue of deep mantle plumes: New results from finite-frequency tomography, *Geochem. Geophys. Geosyst.*, *7*, Q11007, doi:10.1029/2006GC001248.
- Murakami, M., K. Hirose, K. Kawamura, N. Sata, and Y. Ohishi (2004), Post-perovskite phase transition in MgSiO_3 , *Science*, *304*, 855–858, doi:10.1126/science.1095932.
- Nakagawa, T., and P. J. Tackley (2008), Lateral variations in CMB heat flux and deep mantle seismic velocity caused by a thermal-chemical-phase boundary layer in 3D spherical convection, *Earth Planet. Sci. Lett.*, *271*, 348–358, doi:10.1016/j.epsl.2008.04.013.
- Oganov, A. R., and S. Ono (2004), Theoretical and experimental evidence for a post-perovskite phase of MgSiO_3 in Earth's D'' layer, *Nature*, *430*, 445–448.
- Ohta, K., S. Onoda, K. Hirose, R. Sinmyo, K. Shimizu, N. Sata, Y. Ohishi, and A. Yasuhara (2008), The electrical conductivity of post-perovskite in Earth's D'' layer, *Science*, *320*, 89–91.
- Panning, M., and B. Romanowicz (2006), A three-dimensional radially anisotropic model of shear velocity in the whole mantle, *Geophys. J. Int.*, *167*, 361–379, doi:10.1111/j.1365-246X.2006.03100.x.
- Ritsema, J., H. J. van Heijst, and J. H. Woodhouse (2004), Global transition zone tomography, *J. Geophys. Res.*, *109*, B02302, doi:10.1029/2003JB002610.
- Shim, S. H., T. S. Duffy, R. Jeanloz, and G. Shen (2004), Stability and crystal structure of MgSiO_3 perovskite to the core-mantle boundary, *Geophys. Res. Lett.*, *31*, L10603, doi:10.1029/2004GL019639.
- Simmons, N. A., and S. P. Grand (2002), Partial melting in the deepest mantle, *Geophys. Res. Lett.*, *29*(11), 1552, doi:10.1029/2001GL013716.
- Simmons, N. A., A. M. Forte, and S. P. Grand (2009), Joint seismic, geodynamic and mineral physical constraints on three-dimensional mantle heterogeneity: Implications for the relative importance of thermal versus compositional heterogeneity, *Geophys. J. Int.*, *177*, 1284–1304, doi:10.1111/j.1365-246X.2009.04133.x.
- Sleep, N. H. (1990), Hotspots and mantle plumes: Some phenomenology, *J. Geophys. Res.*, *95*, 6715–6736, doi:10.1029/JB095iB05p06715.
- Stackhouse, S., J. P. Brodholt, J. Wookey, J. M. Kendall, and G. D. Price (2005), The effect of temperature on the seismic anisotropy of the perovskite and post-perovskite polymorphs of MgSiO_3 , *Earth Planet. Sci. Lett.*, *230*, 1–10, doi:10.1016/j.epsl.2004.11.021.
- Steinberger, B. (2000), Plumes in a convecting mantle: Models and observations for individual hotspots, *J. Geophys. Res.*, *105*, 11,127–11,152, doi:10.1029/1999JB900398.
- Steinberger, B., and R. Holme (2008), Mantle flow models with core-mantle boundary constraints and chemical heterogeneities in the lowermost mantle, *J. Geophys. Res.*, *113*, B05403, doi:10.1029/2007JB005080.
- Tackley, P. J. (2002), Strong heterogeneity caused by deep mantle layering, *Geochem. Geophys. Geosyst.*, *3*(4), 1024, doi:10.1029/2001GC000167.
- Tateno, S., K. Hirose, N. Sata, and Y. Ohishi (2009), Determination of post-perovskite phase transition boundary up to 4400 K and implications for thermal structure in D'' layer, *Earth Planet. Sci. Lett.*, *277*, 130–136, doi:10.1016/j.epsl.2008.10.004.
- Trampert, J., F. Deschamps, J. Resovsky, and D. Yuen (2004), Probabilistic tomography maps chemical heterogeneities throughout the lower mantle, *Science*, *306*, 853–856, doi:10.1126/science.1101996.
- Tsuchiya, T., J. Tsuchiya, K. Umemoto, and R. A. Wentzcovitch (2004), Phase transition in MgSiO_3 perovskite in the earth's lower mantle, *Earth Planet. Sci. Lett.*, *224*, 241–248, doi:10.1016/j.epsl.2004.05.017.
- van der Hilst, R. D., S. Widiyantoro, and E. R. Engdahl (1997), Evidence for deep mantle circulation from global tomography, *Nature*, *386*, 578–584, doi:10.1038/386578a0.
- van der Hilst, R. D., M. V. de Hoop, P. Wang, S. H. Shim, P. Ma, and L. Tenorio (2007), Seismostratigraphy and thermal structure of Earth's

- core-mantle boundary region, *Science*, 315, 1813–1817, doi:10.1126/science.1137867.
- Wang, Y., and L. X. Wen (2004), Mapping the geometry and geographic distribution of a very low velocity province at the base of the Earth's mantle, *J. Geophys. Res.*, 109, B10305, doi:10.1029/2003JB002674.
- Wentzcovitch, R. M., T. Tsuchiya, and J. Tsuchiya (2006), MgSiO_3 postperovskite at D'' conditions, *Proc. Natl. Acad. Sci. U. S. A.*, 103, 543–546, doi:10.1073/pnas.0506879103.
- Williams, Q., and E. J. Garnero (1996), Seismic evidence for partial melt at the base of Earth's mantle, *Science*, 273, 1528–1530, doi:10.1126/science.273.5281.1528.
- Wookey, J., S. Stackhouse, J. M. Kendall, J. Brodholt, and G. D. Price (2005), Efficacy of the post-perovskite phase as an explanation for lowermost-mantle seismic properties, *Nature*, 438, 1004–1007, doi:10.1038/nature04345.
- Wysession, M. E., T. Lay, J. Revenaugh, Q. Williams, E. J. Garnero, R. Jeanloz, and L. H. Kellogg (1998), The D'' discontinuity and its implications, in *Core-Mantle Boundary Region, Geodyn. Ser.*, vol. 28, edited by M. Gurnis et al., pp. 273–297, AGU, Washington, D. C.
-
- P. Driscoll and B. Wu, Department of Geology and Geophysics, Yale University, New Haven, CT 06520, USA. (benjunwu@gmail.com)
- P. Olson, Department of Earth and Planetary Sciences, Johns Hopkins University, Baltimore, MD 21218, USA.